

A hybrid radial basis function-finite difference method for modelling two-dimensional thermo-elasto-plasticity, Part 1: Method formulation and testing

Gašper Vuga^a, Boštjan Mavrič^{a,b}, Božidar Šarler^{a,b,*}

^a Faculty of Mechanical Engineering, University of Ljubljana, Aškerčeva cesta 6, Ljubljana, SI-1000, Slovenia

^b Institute of Metals and Technology, Lepi pot 11, Ljubljana, SI-1000, Slovenia

ARTICLE INFO

Keywords:

Thermo-mechanical modelling
von Mises small strain plasticity
Hybrid radial basis function generated finite differences
Polyharmonic splines

ABSTRACT

A hybrid version of the strong form meshless Radial Basis Function-Finite Difference (RBF-FD) method is introduced for solving thermo-mechanics. The thermal model is spatially discretised with RBF-FD, where trial functions are polyharmonic splines augmented with polynomials. For time discretisation, the explicit Euler method is employed. An extension of RBF-FD, the hybrid RBF-FD, is introduced for solving mechanical problems. The model is one-way coupled, where temperature affects displacements. The thermo-elastoplastic material response is considered where the stress field is generally non-smooth. The hybrid RBF-FD, where the finite difference method is used to discretise the divergence operator from the balance equation, is shown to be successful when dealing with such problems. The mechanical model is introduced in a plane strain and in a generalised plane strain (GPS) assumption. For the first time, this work presents a strong form RBF-FD for GPS problems subjected to integral form constraints. The proposed method is assessed regarding h -convergence and accuracy on the benchmark with heating an elastoplastic square. It is proven to be successful at solving one-way coupled thermo-elastoplastic problems. The proposed novel meshless approach is efficient, accurate, and robust. Its use in an industrial situation is provided in Part 2 of this paper.

1. Introduction

Computational modelling of thermo-elasto-plasticity represents a continuous field of research since the advent of computers. In contrast to conventional mesh-based discretisation methods like the finite element method (FEM) [1] and finite volume method (FVM) [2], which rely on polygonisation to discretise the domain, meshless methods (MMs) [3–5] eliminate the need for this process. Instead, the discretisation is employed as a cloud of nodes distributed throughout the domain. This approach offers inherent advantages in terms of straightforward geometric adaptivity and flexibility, especially when dealing with intricate geometries and significant distortions [6]. Also, multi-level techniques can simply be applied [7].

In previous works [8,9], weak-form MMs have been successfully demonstrated to solve elasto-plastic problems where the polygonisation of the domain is still needed. This study employs strong-form MM [3], where PDEs are directly discretised in their differential form, and no polygonisation is employed.

The solving of partial differential equations on the cloud of the nodes is based on Local Radial Basis Function Collocation Method

(LRBFCM) [10–12], recently also known as the Radial Basis Function generated Finite Difference (RBF-FD) method [13]. This type of collocation method employs a combination of radial basis functions (RBFs) and monomials to approximate the solution field. The approximation is performed on the overlapping local support stencils prescribed to each node. For the discretisation of differential operators, finite-difference-like weight coefficients are computed by inverting small full systems of equations proportional to the number of nodes in the support domain. In this study, polyharmonic splines (PHSs) are used as RBFs. Combined with polynomials, they guarantee the positive definiteness of a local interpolant. The polynomial order governs the h -convergence, and the accuracy is improved with the number of local support nodes [13]. The free parameters of PHSs are explicitly determined for each support domain and do not require a heuristic search for them as in the case of Gaussian or Multiquadric RBFs.

The RBF-FD method has been previously applied to various scientific and industrial problems, e.g., convective–diffusive solid–liquid phase change [14], natural convection [15], turbulent flow during the process of continuous casting in 2D [16,17] and 3D [18], the influence

* Corresponding author at: Faculty of Mechanical Engineering, University of Ljubljana, Aškerčeva cesta 6, Ljubljana, SI-1000, Slovenia.

E-mail addresses: gasper.vuga@fs.uni-lj.si (G. Vuga), bostjan.mavric@fs.uni-lj.si (B. Mavrič), bozidar.sarler@fs.uni-lj.si (B. Šarler).

of magnetic field on fluid flow [19,20], simulation of macrosegregation in binary metallic casts [21], reaction–diffusion problems on surfaces [22], phase field modelling of dendritic solidification [23] with a space–time adaptive approach [24], micro combustion problems [25], fluid flow in porous media [26], flow of a non-Newtonian fluid [27], compressible viscous flow in a tube [28], financial option valuation [29] to mention a few. A similar type of strong form MM called the localised radial Trefftz collocation method, where basis functions are based on the analytical PDE solution, was successfully applied in steady-state heat conduction (2D and 3D) in functionally graded materials [30]. A comprehensive overview of local MMs can be found in [31].

In terms of mechanics, the use of RBF-FD was successfully demonstrated on linear elastic benchmarks [10,11,32], composite plates response [33], natural frequencies of beams and plates [34], thermo-elasticity benchmarks [35,36], stresses and strains in solidified part during direct-chill casting of aluminium [37], and shape determination in hot rolling of steel [38–41], where all studies were performed in 2D with the use of multiquadric RBFs. The use of PHSs was included in studies of elastic benchmarks [6], the elastic response of thoracic diaphragm [42], the elasto-plastic benchmark [43], and the mechanical slice model of continuous casting of steel [44]. In the nonlinear mechanical studies [37,44], the Jacobian was determined numerically, which resulted in slow convergence. In [43], only elastic material parameters were used for composing Jacobian, resulting in many nonlinear iterations. Similarly, in [41], where the ideal plastic model was used, the direct iteration method was employed for solving the system of equations.

This work solves the thermo-mechanical model as a one-way coupled, where a temperature solution is applied to the mechanical model as a thermal load. The heat diffusion is solved by the RBF-FD using augmented PHSs. It was found in [45] that the classical RBF-FD cannot cope successfully with the elasto-plastic cases since it produces an oscillatory solution. Spatial discretisation is performed with a hybrid RBF-FD that combines the finite difference method (FDM) and RBF-FD. Stresses and strains are discretised with RBF-FD on finite difference stencils prescribed to each collocation node where basis functions are augmented PHSs. Then, the divergence operator in the balance equation is discretised with the FDM. This method sufficiently overcomes the problem of differentiation of non-smooth field (stress). To stabilise Neumann boundary conditions (BCs), a simple shift of boundary nodes in the opposite direction of the outward-facing normal is performed when evaluating the gradient operators. A global system of nonlinear equations is solved with a Newton–Raphson iteration algorithm. The return mapping algorithm (RMA) is employed for solving rate-independent thermo-elasto-plastic constitutive equations and computation of consistent tangent operator (CTO). The method is applied in two dimensions in plane strain (PS) and in generalised plane strain (GPS) assumptions. In Part 2 of this paper, the method is further extended and applied to a real-life industrial example.

The main originality of this work represents the derivation, implementation and validation of a hybrid RBF-FD for solving thermo-elasto-plastic problems within a plane strain (PS) and a generalised plane strain (GPS) assumptions. With the GPS, this study, for the first time, employs RBF-FD that includes integral form constraints.

The present paper is structured in the following order. The governing equations of the thermal and mechanical models are given in Section 2. Numerical methods needed for discrete solving of a thermal model are presented in Section 3, and for a mechanical model in Section 4. Validation of the introduced procedure is presented in Section 5, and lastly, the conclusions are provided in Section 6.

2. Physical model

2.1. Thermal model

Governing equation of the thermal model is expressed by the heat diffusion

$$\frac{\partial \mathcal{H}}{\partial t} = \nabla k \cdot \nabla T + k \nabla^2 T, \quad (1)$$

where $\mathcal{H} = \rho c_p T$ is volume-specific enthalpy and ρ, c_p, T , and k stand for density, specific heat at constant pressure, temperature, and thermal conductivity, respectively. To obtain a unique solution, different boundary conditions (BSc) are applied at the boundary $\Gamma = \Gamma_D \cup \Gamma_N$

$$\begin{aligned} T &= \hat{T} & \text{on } \Gamma_D, \\ \mathbf{q} \cdot \mathbf{n} &= \hat{q}_n & \text{on } \Gamma_N, \end{aligned} \quad (2)$$

where on Γ_D temperature is prescribed as \hat{T} and on Γ_N heat flux \mathbf{q} in normal direction \mathbf{n} is prescribed as \hat{q}_n . Heat flux is defined by the Fourier's law $\mathbf{q} = -k \nabla T$. When $\hat{q}_n = 0$, the boundary is considered to be thermally insulated. Since the thermal problem is time-dependent, an initial temperature must be imposed as $T(t=0) = \hat{T}_0$.

2.2. Mechanical model

Here the basics of isotropic small-strain von Mises plasticity are shortly revised. The mechanical equilibrium is posed by the balance law

$$\nabla \cdot \boldsymbol{\sigma} = -\mathbf{f}, \quad (3)$$

where $\boldsymbol{\sigma}$ is the stress tensor and \mathbf{f} is the body force vector. The strain tensor is within a small strain approximation defined in terms of displacement \mathbf{u} as

$$\boldsymbol{\varepsilon} = 1/2 (\nabla \mathbf{u} + \nabla \mathbf{u}^\top) = \nabla^s \mathbf{u}, \quad (4)$$

where ∇^s represents the symmetric gradient operator. Within the small strain assumption, the total strain can be additively split into elastic, plastic and thermal parts as $\boldsymbol{\varepsilon} = \boldsymbol{\varepsilon}^e + \boldsymbol{\varepsilon}^p + \boldsymbol{\varepsilon}^{th}$. Thermal strain is defined as $\boldsymbol{\varepsilon}^{th} = \alpha(T - T_{ref})\mathbf{I}$, where α stands for linear expansion coefficient, T_{ref} for the reference temperature and \mathbf{I} for the identity tensor. The relationship between stresses and strains is defined by the Hooke's law

$$\boldsymbol{\sigma} = \mathbf{D}^e : (\boldsymbol{\varepsilon} - \boldsymbol{\varepsilon}^p - \boldsymbol{\varepsilon}^{th}), \quad (5)$$

where \mathbf{D}^e stands for the fourth-order elasticity tensor. It can be defined in terms of only two independent material properties for isotropic material, for example, with Lamé constants (G, λ) or with Young's modulus and Poisson ratio (E, ν). If the response is totally recoverable, plastic strain equals zero, and the relation (5) is enough to determine stresses. Additional conditions and evolution equations must be satisfied if the plastic strain is nonzero. The first one is the yield criterion. It gives the critical stress where the material starts yielding. The employed von Mises yield criterion states that the material yields when von Mises stress $\sigma_{vm} = \sqrt{3J_2(s)}$ exceeds the yield stress $\sigma_y = \sigma_y(T, \bar{\varepsilon}^p)$ obtained from the uni-axial tensile test. Scalar J_2 represents the second invariant of the deviatoric part of the stress tensor $s = \boldsymbol{\sigma} - \text{tr}(\boldsymbol{\sigma})/3$. A simple isotropic hardening is assumed where the evolution of yield stress is governed only by temperature and accumulated plastic strain $\bar{\varepsilon}^p = \sqrt{\frac{2}{3}} \|\boldsymbol{\varepsilon}^p\|$. The evolution is specified by a hardening curve which has a typical form of $\sigma_y(T, \bar{\varepsilon}^p) = \sigma_{y0}(T) + \kappa(T, \bar{\varepsilon}^p)$ where σ_{y0} stands for the initial yield stress and κ for a generally nonlinear function. In this work, the hardening curve is simplified as $\sigma_y(\bar{\varepsilon}^p) = \sigma_{y0} + H \bar{\varepsilon}^p$, where H stands for the hardening modulus. Next, admissible stress states are compactly given by a yield function Φ that uses the von Mises yield criteria

$$\Phi(\boldsymbol{\sigma}, \sigma_y) = \sqrt{3J_2(s(\boldsymbol{\sigma}))} - \sigma_y, \quad (6)$$

where $\Phi < 0$ in elastic regime and $\Phi = 0$ in plastic regime. The evolution of plastic strain is given by the plastic flow rule

$$\dot{\epsilon}^p = \dot{\gamma} \frac{\partial \Phi}{\partial \sigma} = \dot{\gamma} \sqrt{\frac{3}{2}} \frac{s}{\|s\|}, \quad (7)$$

where γ represents the plastic multiplier. It provides the magnitude of the plastic strain and connects the stress space with the strain space. The evolution of accumulated plastic strain is equivalent to the evolution of the plastic multiplier

$$\dot{\epsilon}^p = \dot{\gamma}. \quad (8)$$

Finally, a set of Kuhn–Tucker conditions specifies when the evolution of plastic strain and internal variables may occur

$$\Phi(\sigma, \kappa) \leq 0, \quad \dot{\gamma} \geq 0, \quad \Phi(\sigma, \kappa) \dot{\gamma} = 0. \quad (9)$$

A more in-depth explanation of the described equations can be found in [1].

2.2.1. Boundary conditions

To obtain a unique solution of the mechanical model in terms of displacements $\mathbf{u}(\mathbf{p})$ where \mathbf{p} is the position vector, a set of boundary conditions (BCs) is applied. Three different mechanical BC types are introduced at the boundary $\Gamma = \Gamma_u \cup \Gamma_T \cup \Gamma_F$

$$\begin{aligned} \mathbf{u} &= \hat{\mathbf{u}} && \text{on } \Gamma_u, \\ \boldsymbol{\sigma} \cdot \mathbf{n} &= \hat{\mathbf{T}} && \text{on } \Gamma_T, \\ \{u_n, T_t\} &= \{0, 0\} && \text{on } \Gamma_F, \end{aligned} \quad (10)$$

where on Γ_u displacement $\hat{\mathbf{u}}$ is prescribed, on Γ_T traction vector $\hat{\mathbf{T}}$ is specified and on the symmetry boundary part Γ_F displacement in the direction of the normal u_n and traction in a tangential direction $T_t = \mathbf{T} \cdot \mathbf{t}$ is set to zero.

2.2.2. Generalised plane strain model

Within a generalised plane strain assumption, the strain component perpendicular to the observed (here x - y) plane is set to be of a linear form

$$\epsilon_{zz}(x, y) = ax + by + c. \quad (11)$$

With this definition, three new unknowns are introduced (a, b, c), solved from the three additional equations

$$\begin{aligned} N_z &= \int_{\Omega} \sigma_{zz} d\Omega, \\ M_x &= \int_{\Omega} \sigma_{zz} y d\Omega, \\ M_y &= \int_{\Omega} \sigma_{zz} x d\Omega, \end{aligned} \quad (12)$$

where N_z represents the force in the longitudinal direction, M_x momentum around the x -axis, M_y momentum around the y -axis, and Ω the domain of observation. All values in (12) are set to zero $\{\hat{N}_z, \hat{M}_x, \hat{M}_y\} = \{0, 0, 0\}$.

3. Numerical solution procedure of the thermal model

3.1. Temporal discretisation

Time marching of the heat diffusion equation is performed using the explicit Euler scheme that is first-order accurate in time step Δt . The time derivative at t_0 is discretised as

$$\frac{\partial \mathcal{H}}{\partial t} \Big|_{t_0} = \frac{\mathcal{H}^{t_0+\Delta t} - \mathcal{H}^{t_0}}{\Delta t}. \quad (13)$$

A sufficiently small time step should be employed for the scheme to be stable. In finite difference method for a 2D heat diffusion problem its maximum time step is $\Delta t_{max} < h^2/4D$, where h and D define a space between nodes on regular node arrangement and $D = k/\rho c_p$ thermal diffusivity, respectively. In this work, the stable time step is defined as $\Delta t = \alpha_{\Delta t} \Delta t_{max}$, where $\alpha_{\Delta t}$ is the time stability parameter.

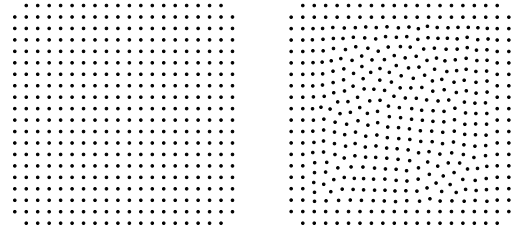


Fig. 1. Regular (left) and scattered (right) node arrangement on the unit square.

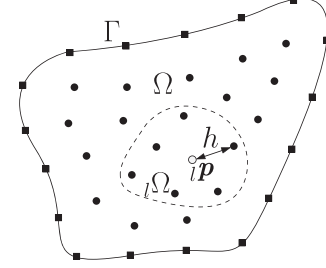


Fig. 2. Scheme of a generic domain Ω with boundary Γ . The solid circles and squares represent interior and boundary nodes, respectively. The empty circle represent the centre node ${}_i p$ of the subdomain ${}_i \Omega$ where the minimum distance between nodes is denoted with h .

3.2. Spatial discretisation

In this work, the RBF-FD method is employed for spatial discretisation. The method generalises the traditional finite difference (FD) method. It estimates the spatial differential operator (DO) at a collocation node (CN) as a weighted sum of field values. While the standard FD method only works with regular node arrangements (RNAs), RBF-FD can easily handle scattered node arrangements (SNAs). This allows for solutions to problems with complex geometries but comes at the cost of calculating separate weights for each discretisation node. Fig. 1 illustrates an example of both RNA and SNA on the unit square. The corner nodes are left out to prevent the possible boundary condition mismatch problem. The procedure of scattered node positioning used here is based on the node repelling algorithm, initially presented in [46] and elaborated in [37].

3.2.1. Local interpolation problem

The generic domain Ω with boundary Γ , which is discretised into N nodes, is shown in Fig. 2. To construct a local interpolant, the local subdomain ${}_i \Omega$ centred at the node ${}_i p$ ($i = 1, \dots, N$) must be defined. The use of the previously described node-repelling algorithm leads to a homogeneously isotropic node discretisation, so the selection of ${}_i \Omega$ simply includes the centre node ${}_i p$ and ${}_i N - 1$ nearest neighbours.

The RBF-FD method uses radial basis functions (RBFs) for trial functions at each of the subdomains. In this work, a special type of RBFs are used — polyharmonic splines (PHSs) [13]. Compared to other RBFs, such as Gaussian or Multiquadrics, those do not require a complicated and time-consuming optimal shape parameter determination, making them attractive to work with. PHS function defined on ${}_i \Omega$ and centred at the ${}_i p_i$, where $i = 1, \dots, {}_i N$, has a dimensionless form of

$${}_i \Phi_i(\mathbf{p}) = \left(\frac{\|\mathbf{p} - {}_i p_i\|}{{}_i h} \right)^m, \quad m = 1, 3, 5, \dots \quad (14)$$

where m represents the order of PHS and ${}_i h$ the average distance from the central node, defined as

$${}_i h = \sqrt{\frac{\sum_{i=2}^{{}_i N} \|\mathbf{p} - {}_i p_i\|^2}{{}_i N - 1}}}. \quad (15)$$

It holds for all types of RBFs that the stagnation error does not decrease under refinement. In [13], it was demonstrated that augmenting the PHS interpolant with polynomials results in a decrease in the stagnation error. It was also shown that the order of augmentation p also governs the order of h -convergence [13]. To obtain p th order of convergence, it should hold that $m < p$ and ${}_iN \gtrsim 2M$, where $M = \binom{p+n_d}{p}$.

An augmented RBF interpolant inside ${}_i\Omega$ of a general function ${}_i y_\xi(p)$ where $\xi = 1, \dots, n_d$ runs over n_d space dimensions can be written as

$${}_i y_\xi(p) \approx \sum_{i=1}^{iN} {}_i \alpha_{i,\xi} {}_i \Phi_i(p) + \sum_{i=1}^M {}_i \alpha_{(iN+i),\xi} p_i(p) = \sum_{i=1}^{iN+M} {}_i \alpha_{i,\xi} {}_i \Psi_i(p). \quad (16)$$

where ${}_i \alpha_{i,\xi}$, $i = 1, \dots, iN + M$ are the interpolation coefficients, $p_i(p)$, $i = 1, \dots, M$ represents monomials and $\Psi_i(p)$ the complete set of basis functions, either RBFs ($i \leq iN$) or monomials ($i > iN$). This local interpolation problem can be written as a linear system of $n_d(iN + M)$ equations

$$\sum_{\chi=1}^{n_d} \sum_{i=1}^{iN+M} {}_i A_{ji,\xi\chi} {}_i \alpha_{i,\chi} = {}_i \gamma_{j,\xi}, \quad (17)$$

where the interpolation matrix is defined as

$${}_i A_{ji,\xi\chi} = \begin{cases} \Psi_i({}_i p_j) \delta_{\xi\chi} & \text{if } {}_i p_j \in \Omega \\ B_{\xi\chi}({}_i p_j) \Psi_i({}_i p_j) & \text{if } {}_i p_j \in \Gamma \\ p_{j-iN}({}_i p_i) \delta_{\xi\chi} & \text{if } j > iN \text{ and } i \leq iN \\ 0 & \text{otherwise} \end{cases}, \quad (18)$$

and the vector of known values as

$${}_i \gamma_{j,\xi} = \begin{cases} y_\xi({}_i p_j) & \text{if } {}_i p_j \in \Omega \\ b_\xi({}_i p_j) & \text{if } {}_i p_j \in \Gamma \\ 0 & \text{otherwise.} \end{cases} \quad (19)$$

where for the points on the Γ , the linear boundary condition is imposed $\sum_{\xi} B_{\xi\chi}({}_i p_j) y_\xi({}_i p_j) = b_\chi({}_i p_j)$, where B and b are the linear boundary operator and the boundary value, respectively.

3.2.2. Discretisation of differential operators

Applying a differential operator \mathcal{L} on the interpolant results in

$$\mathcal{L} {}_i y(p)_\xi = \sum_{\chi=1}^{n_d} \mathcal{L}_{\xi\chi} {}_i y_\chi(p) \approx \sum_{\chi=1}^{n_d} \sum_{i=1}^{iN+M} {}_i \alpha_{i,\chi} \mathcal{L}_{\xi\chi} {}_i \Psi_i(p), \quad (20)$$

where one can see that the operator is acting only on the basis functions. Expressing the interpolation coefficients from Eqs. (17)–(19), it can be written in the following form

$$\begin{aligned} \mathcal{L} {}_i y(p)_\xi &\approx \sum_{\zeta=1}^{n_d} \sum_{j=1}^{iN+M} {}_i \gamma_{j,\zeta} \sum_{\chi=1}^{n_d} \sum_{i=1}^{iN+M} {}_i A_{ij,\chi\zeta}^{-1} \mathcal{L}_{\xi\chi} {}_i \Psi_i(p) \\ &\approx \sum_{\zeta=1}^{n_d} \sum_{j=1}^{iN+M} {}_i \gamma_{j,\zeta} {}_i \mathcal{W}_{j,\xi\zeta}(p). \end{aligned} \quad (21)$$

where the operator's action on a function is now expressed as a weighted sum of known values ${}_i \gamma_{j,\zeta}$ and operator coefficients ${}_i \mathcal{W}_{j,\xi\zeta}(p)$. The similarity with the FD method is evident here, where the operator coefficients are pre-determined. In RBF-FD, these coefficients have to be calculated for each node initially, but they remain constant throughout the simulation.

The introduced procedure is utilised to discretise the gradient and Laplace operator of scalar fields present in the governing equation (1).

4. Numerical solution procedure of the mechanical model

4.1. Incremental solution

Since the mechanical problem is history-dependent, it is solved incrementally. This means that the external load is applied in increments.

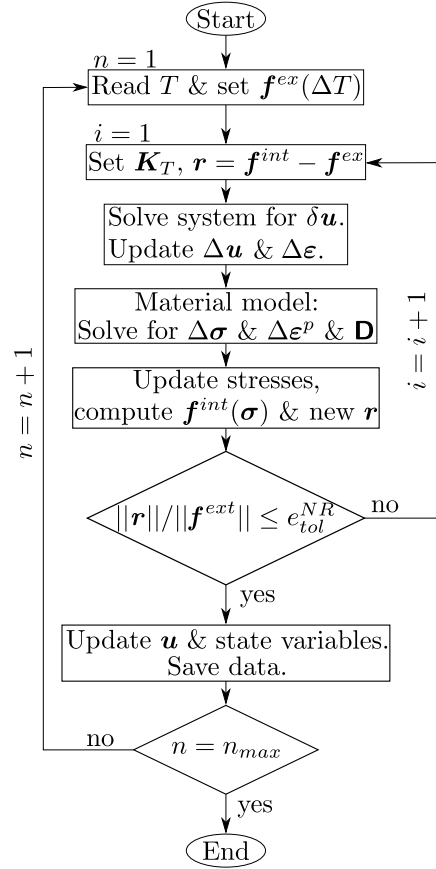


Fig. 3. Flowchart of the mechanical model.

For a $(n + 1)$ th load increment, the governing Eq. (3) can be written as $f^{int}|_{n+1} - f^{ex}|_{n+1} = r(u_{n+1}) = 0$, where f^{int} represents internal force defined as $f^{int} = \nabla \cdot \sigma(\nabla^s u)$, f^{ex} external load and r the residual that should be zero. Due to a nonlinear relationship between stresses and strains, the residual is linearised as

$$\nabla \cdot (\mathbf{D}\nabla^s) \Big|_{n+1}^{i-1} \delta u = -r|_{n+1}^{i-1}, \quad (22)$$

where $\mathbf{K}_T = \nabla \cdot (\mathbf{D}\nabla^s)$ represents stiffness matrix with $\mathbf{D} = \partial\sigma/\partial\varepsilon$. Eq. (22) is iteratively (index i) solved for δu . Then, the displacement increment is updated as $\Delta u^i = \Delta u^{i-1} + \delta u$, and strain increment $\Delta \varepsilon^i$ is determined by Eq. (4). This is then inserted into the integration model, where all other state variables are computed by solving Eqs. (5)–(9). For the integration of the constitutive relations, the Return Mapping Algorithm (RMA) is used here, where integration is performed implicitly [1]. From the result of stress, the internal force and the residual is calculated. If the condition $\|r|_{n+1}^i\| / \|f^{ext}|_{n+1}\| \leq e_{tol}^{NR}$, where e_{tol}^{NR} represents equilibrium convergence tolerance, is satisfied, the displacement is updated as $u_{n+1} = u_n + \Delta u^i$ (and similarly all other state variables.)

Since only thermal load is applied here, the external force is defined in terms of a temperature difference as $f_{n+1}^{ex} = \nabla \cdot ((3\lambda + 2G)\varepsilon^{th})|_{n+1} = \nabla \cdot ((3\lambda + 2G)\alpha\Delta T \mathbf{I})|_{n+1}$, where $\Delta T = T_{n+1} - T_n$. The flowchart of the described procedure is shown in Fig. 3.

4.2. Spatial discretisation

Governing equation (22) is discretised with a hybrid RBF-FD method. Here the term $(\mathbf{D}\nabla^s)$ is not evaluated in CN but on a regular finite difference stencil prescribed to each CN. 2nd order FD stencils used here are shown in Fig. 4 (crosses). The divergence operator in

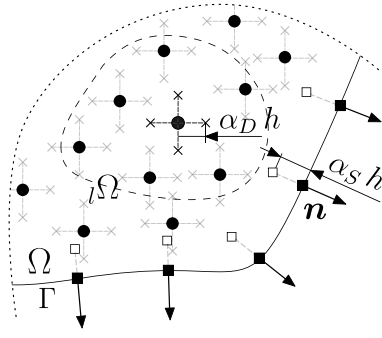


Fig. 4. Discretisation of the domain Ω section used for the mechanical model.

CN is then expressed with the FDM. As shown in the figure, the distance between CN and a node on the FD stencil is defined as the product of an FD stencil size parameter α_D and inter-nodal spacing h . The discretisation of the divergence operator in f^{ex} is also performed via the FDM. Due to that, the temperature difference field, which is calculated in the CNs, must be interpolated on the FD stencils. Compared to the classical RBF-FD, the downside of the hybrid RBF-FD is that material iteration, where stresses are computed, is executed in 4 times more nodes, i.e. in each FD node on an FD stencil assigned to each CN.

As opposed to the thermal model where BCs are included inside the local interpolation (Eqs. (18), and (19)), it was found that the introduced mechanical model performs better when BCs are not included inside local interpolation but as a part of the global system of equations. All nodes are treated as inner nodes when computing the coefficients. For the boundary conditions to be stabilised, a simple stabilisation technique is employed where coefficients are not evaluated in boundary CNs but on virtually shifted nodes inside the domain, shown in Fig. 4 with empty squares. These nodes are positioned in the opposite side of the outward-facing normal vectors for a distance of $\alpha_S h$, where α_S is called the boundary stabilisation parameter.

The integrals, in additional equations for GPS, are discretised similarly as in a midpoint rule, where $\int y(p)dA \approx \sum_{i=1}^N y(p_i)\Delta A_i$. Given the domain area \hat{A} , an area error index is computed as $\alpha_A = \hat{A} / \sum_{i=1}^N \Delta \tilde{A}_i$ where an approximation for the differential area is $\Delta \tilde{A}_i = h_i/\theta$ on inner nodes and $\Delta \tilde{A}_i = h_i/(2\theta)$ on boundary nodes. Then $\Delta A_i \approx \alpha_A \Delta \tilde{A}_{i2}$ for $i \in [1, N]$. The geometric factor $\theta = 1$ for RNA and $\theta = \sqrt{2/\sqrt{3}}$ for SNA. Domain area \hat{A} is computed as the area of the polygon defined by all boundary nodes. The discrete values of $y(p_i)$ are evaluated in CNs.

5. Numerical results

5.1. Problem definition

The proposed method is tested with a simple square benchmark with a side length of L , shown in Fig. 5. On the left and bottom sides of the square, the symmetry BCs are imposed, specifying zero heat fluxes and free-slip BCs. On the other two boundaries, constant heat flux is posed with material free to move — zero traction vector. At time zero, constant temperature is prescribed over the region, and no stresses or strains are present.

The problem is first solved in terms of temperature up to time t_{end} . Then, the solution is applied as a load on the mechanical model where plane strain and generalised plane strain descriptions with linear hardening are assumed. The parameters used are listed in Table 1.

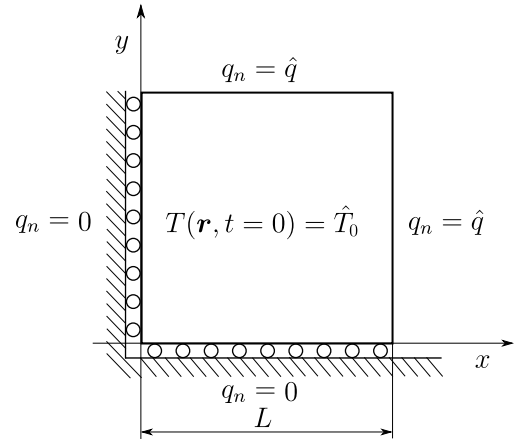


Fig. 5. Scheme of the thermo-mechanical benchmark with geometry and initial and boundary conditions.

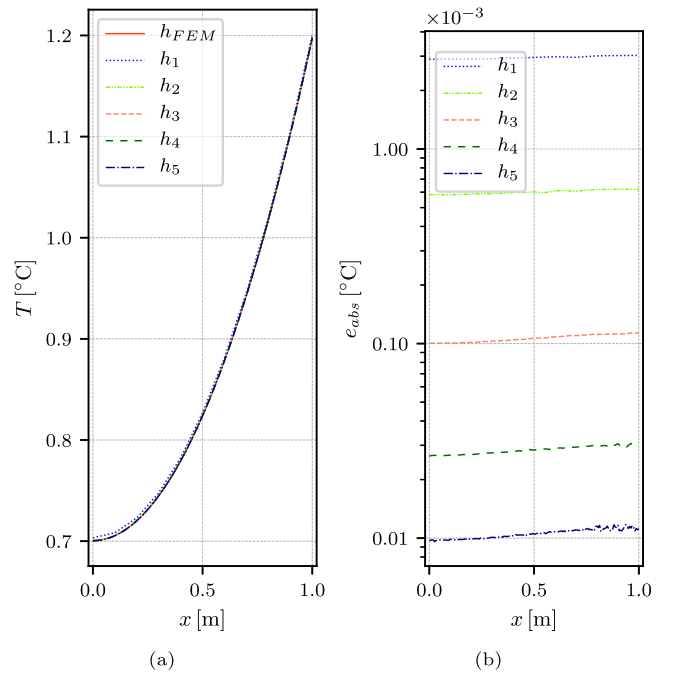


Fig. 6. SNA results of a temperature over line $y = 0.25$ m (a) with corresponding absolute errors (b).

Table 1

Benchmark parameters.

Computational domain	Unit	Value
Size of the domain (L)	m	1
Thermal problem		
Density (ρ)	kg/m ³	1
Specific heat (c_p)	J/kg K	1
Thermal conductivity (k)	W/m K	1
Initial temperature (\hat{T}_0)	°C	0
Prescribed heat flux (\hat{q})	W/m ²	-1
Observed time (t_{end})	s	0.5
Mechanical problem		
Young's modulus (E)	Pa	1
Poisson's ratio (ν)	/	0.3
Linear expansion coefficient (α)	K ⁻¹	0.5
Initial yield stress (σ_{y0})	Pa	0.1
Hardening modulus (H)	Pa	0.1

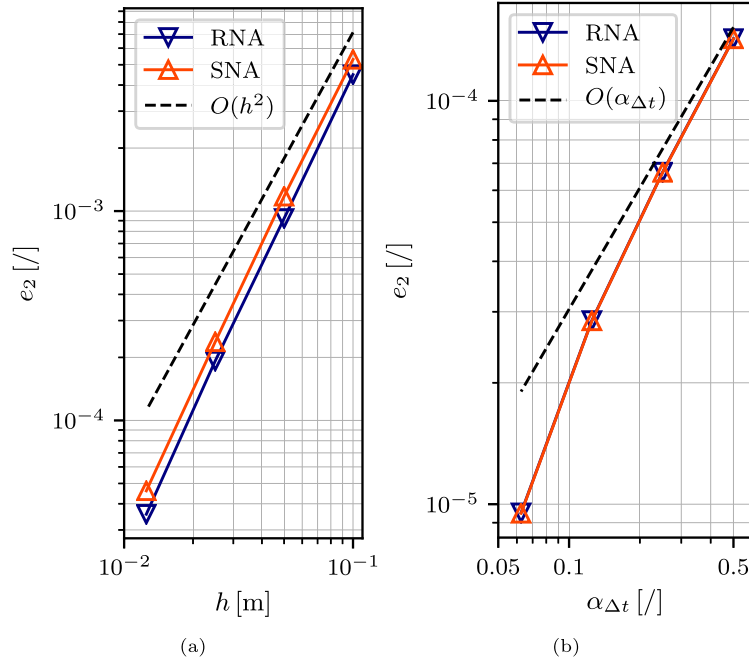


Fig. 7. Convergence of the thermal model. (a): h -convergence for RNA and SNA with fixed time step defined for reference case with h_5 . (b): convergence in $\alpha_{\Delta t}$. The solution is obtained using h_3 .

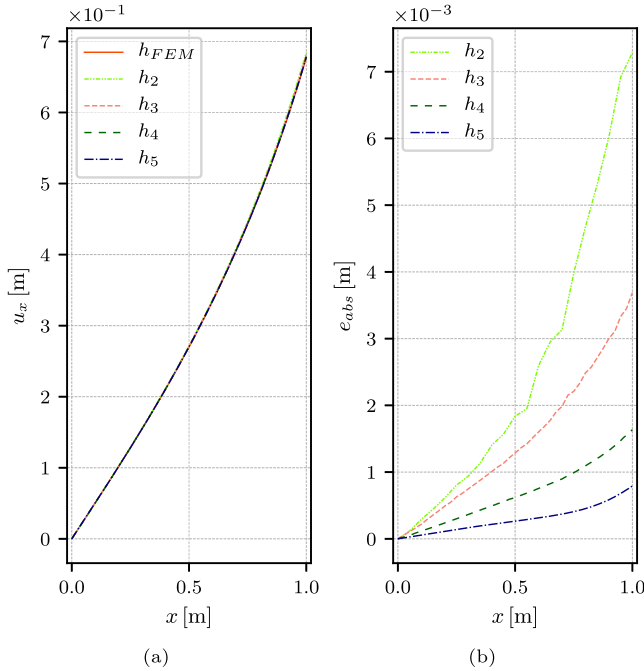


Fig. 8. SNA results of u_x over line $y = 0.25$ m (a) with corresponding absolute errors (b) for a plane strain case.

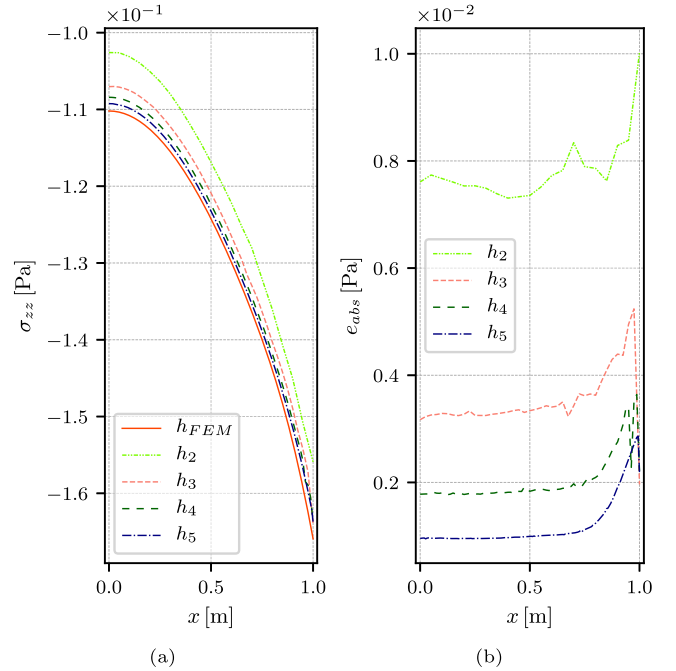


Fig. 9. SNA results of σ_{zz} over line $y = 0.25$ m (a) with corresponding absolute errors (b) for a plane strain case.

5.2. Simulation procedure

The problem is investigated on RNAs and SNAs. Different node arrangement densities are applied with node spacings of $h_i = 0.1/2^{i-1}$ m, $i \in \{1, \dots, 5\}$, where the example with h_2 can be seen in Fig. 1. Numerical parameters specific to the thermal and mechanical model are listed in Table 2. To avoid problems with the evaluation of the 2nd order derivatives in the thermal model (Laplacian operator in Eq. (1)), the order of PHS is $m = 5$. In the mechanical model, only 1st order

derivatives are discretised, so $m = 3$ is chosen. Generally speaking, it was proven in [13] that the order of PHS has practically no effect on accuracy and stability. We observed that the maximum value of the time stability parameter $\alpha_{\Delta t}$ should be 0.5 for the Euler scheme to be stable. The temperature difference applied as an external load on the mechanical model is $\Delta T_{t+\Delta t_{mech}} = T_{t+\Delta t_{mech}} - T_t$, where $\Delta t_{mech} = t_{end}/100$.

The reference solution (RS) was obtained with a finite element code [47]. Linear quadrilateral elements were used with 4 integration nodes within each element. The size of the element edge h_{FEM} was

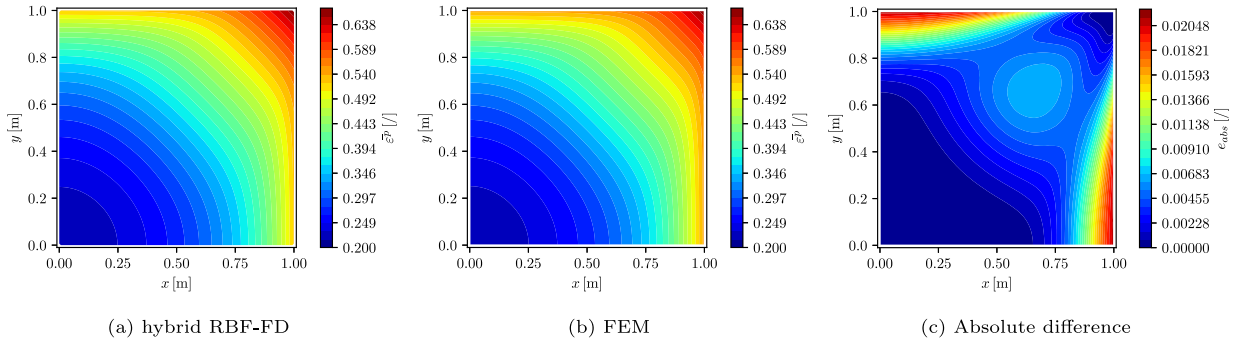


Fig. 10. Accumulated plastic strain solution for PS. (a): SNA with h_5 . (b): reference solution obtained with FEM. (c): Absolute difference between solutions.

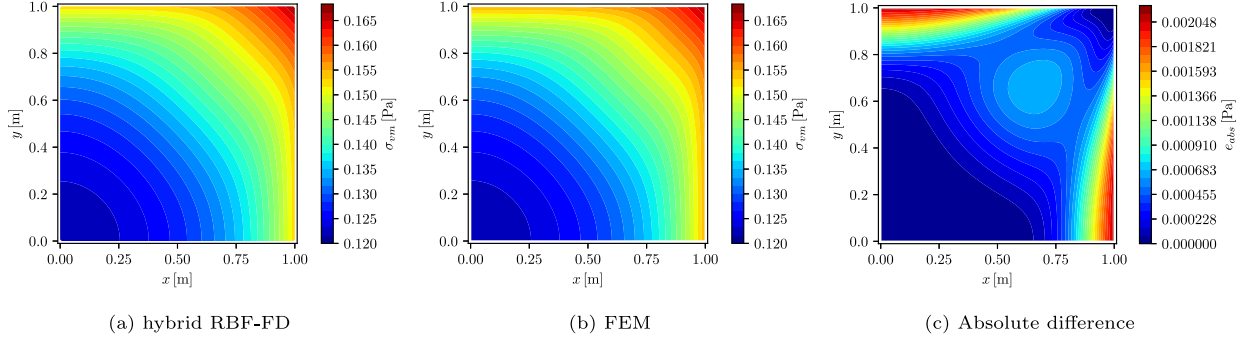


Fig. 11. Von Mises stress solution for PS. (a): SNA with h_5 . (b): reference solution obtained with FEM. (c): Absolute difference between solutions.

Table 2

Numerical parameters.

Thermal problem	
PHS power (m)	5
augmentation order (p)	2
number of nodes in the support domain (${}_iN$)	13
time stability parameter (α_{dt})	0.5
Mechanical problem	
PHS power (m)	3
augmentation order (p)	2
number of nodes in the support domain (${}_iN$)	13
FD stencil size parameter (α_D)	0.5
boundary stabilisation parameter (α_S)	0.1
N-R convergence tolerance (ϵ_{tol}^{NR})	10^{-7}
max number of N-R iterations (NRI_{max})	50

specified as $h_{FEM} = h_5$, where h_5 represents the finest node spacing. The same geometry (Fig. 4), material parameters (Table 1), time stepping ($\alpha_{dt} = 0.5$) and load stepping ($\Delta t_{mech} = t_{end}/100$) were used as in our solution on RNA with h_5 .

The simulation procedure is numerically implemented in the Fortran 2018 programming language and compiled with Intel Fortran Compilers Classic 2021.1.1. Computation was carried out on a personal computer equipped with an Intel(R) Core(TM) i7-8750H CPU containing six cores with a maximum clock speed of 4.10 GHz.

5.3. Thermal response

In Fig. 6, the SNA solution of a temperature along the x -axis at $y = 0.25$ m is shown. For a better distinction, an absolute error $e_{abs}(x) = |T_{FEM}(x) - T(h_i, x)|$ is added. It can be seen that the solution converges with the decrease in h .

To test the convergence of the method, we employ a relative L_2 norm e_2 as

$$e_2 = \sqrt{\frac{\sum_{i=1}^N (T_i - \hat{T}_i)^2}{\sum_{i=1}^N \hat{T}_i^2}} \quad (23)$$

where \hat{T} represents the exact solution and index i runs over all nodes N .

For the h -convergence study, we assume $\hat{T} = T(h_5)$ where all other solutions $T(h_i), i \in \{1, \dots, 4\}$ are computed with a fixed time step as defined for $T(h_5)$. In Fig. 7 (a), the relative error is plotted as a function of node spacing h . One can see that the second-order convergence is obtained as expected when the second-order polynomial augmentation is used. A slight difference can be observed between SNA and RNA.

The convergence regarding the time step is investigated in a case with h_3 . Values of the time stability parameter are chosen as $\alpha_{dt,i} = 0.5/2^{i-1}$ where $i \in \{1, \dots, 5\}$. The exact solution is assumed to be $\hat{T} = T(\alpha_{dt,5})$. In Fig. 7 (b), a relative error is plotted as a function of the time stability parameter. No noticeable change in error between RNA and SNA is observed. As expected, the first-order convergence is obtained.

5.4. Mechanical solution

5.4.1. Plane strain solution

The results of displacement in x direction u_x are shown in Fig. 8, and stress in the direction perpendicular to the x - y plane σ_{zz} in Fig. 9. Similarly, as in the previous section, an absolute error $e_{abs}(x) = |y_{FEM}(x) - y(h_i, x)|$, where y is u_x or σ_{zz} , is added, and the results on h_1 are omitted.

It is evident from the results that the solution is converging to the RS. The error in u_x has zero value at $x = 0$ m since the Dirichlet condition is exactly satisfied and then smoothly increases with x . One order larger difference is observed in σ_{zz} . It is mostly constant, and oscillations increase near $x = 1$ m. These oscillations result from the discontinuous $\Delta T(p)$ used in the mechanical model. Values are discontinuous because the actual solution from the thermal model of $T(p)|_r$ is applied on shifted boundary nodes in the mechanical model.

Figs. 10 and 11 show accumulated plastic strain and von Mises stress over the field, respectively. Solutions are plotted for a hybrid RBF-FD case with SNA and h_5 , and an RS case with $h_{FEM} = h_5$. The absolute value of the difference between the solutions is additionally shown. It can be seen that, in terms of $\bar{\epsilon}^p$, the maximum difference is $\sim 2\%$ and in terms of σ_{vm} it is $\sim 0.2\%$.

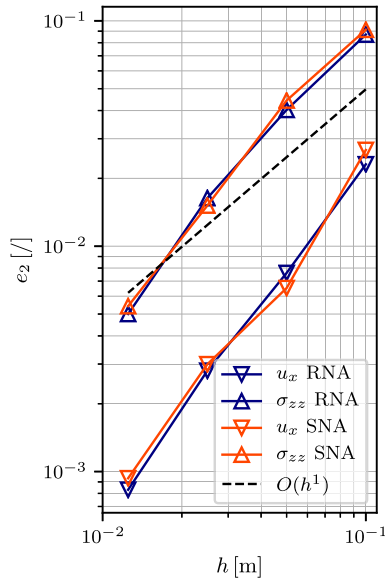


Fig. 12. h -convergence in u_x and σ_{zz} with RNA and SNA for plane strain case.

The convergence behaviour is studied similarly to the thermal model, where the relative error is defined with Eq. (23). Again, the exact solution is assumed to be obtained with h_5 . The temperature values in Eq. (23) are replaced with u_x and σ_{zz} . In [45] it was found that if $\alpha_S \gtrsim 0.25$, the maximum first order of convergence is expected to be obtained. Since the 2nd order of augmentation is used, the second order of convergence is expected to be observed if $\alpha_S = 0$. In Fig. 12, it can be seen that since $\alpha_S > 0$, the order of convergence is not the same as the order of augmentation, but it is also not one order less because $\alpha_S < 0.25$ is used. The convergence order is similar in u_x and σ_{zz} . No significant change can be seen between RNA and SNA solutions.

5.4.2. Generalised plane strain solution

As in the previous case, the solutions computed on SNAs are shown over the line $y = 0.25$ m for u_x in Fig. 13 and for σ_{zz} in Fig. 14. Similar behaviour can be seen in terms of u_x . The shape of σ_{zz} is now different where also tensile stresses are present in the longitudinal direction. Similar oscillatory behaviour in the error of σ_{zz} near $x = 1$ m can be seen. As opposed to the PS case, the error in stress stays in the same range as the error in displacement. Since the material is now free to move in the longitudinal direction, lower values of displacement and stress are obtained, as in the PS case.

A smaller amount of accumulated plastic strain is also induced where most of the area stays in the elastic region, as shown in Fig. 15. Also, smaller values of von Mises stress are obtained, as shown in Fig. 16. It can be seen that in terms of $\bar{\epsilon}^p$ the maximum difference is $\sim 0.19\%$ and in terms of σ_{vm} it is $\sim 0.12\%$.

In Fig. 17, the h -convergence is presented. For the case of RNAs, the convergence behaviour is similar to the PS case. For SNAs, the precision in u_x is a bit lower than for RNA. The difference between RNAs and SNAs is clearly seen in terms of stress. With SNAs, the order of convergence is reduced and gets close to the first order. This might result from lower accuracy when computing the integral equations where area differentials are not computed as accurately as in the RNA.

6. Conclusions

This work presents the RBF-FD and the modified hybrid RBF-FD methods for solving one-way coupled thermo-mechanics for the first time. The hybrid RBF-FD method is modified to be capable of solving thermo-elasto-plastic models. The generalised plane strain state is for

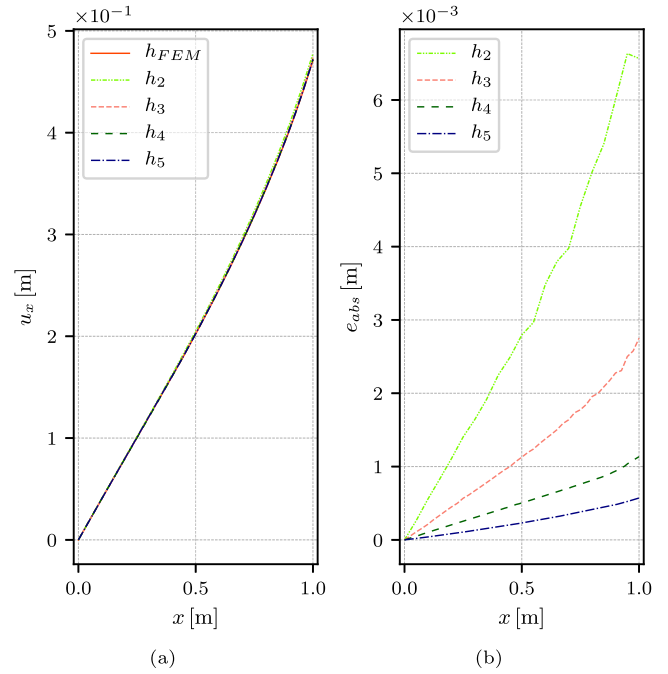


Fig. 13. SNA results of u_x over line $y = 0.25$ m (a) with corresponding absolute errors (b) for a generalised plane strain case.

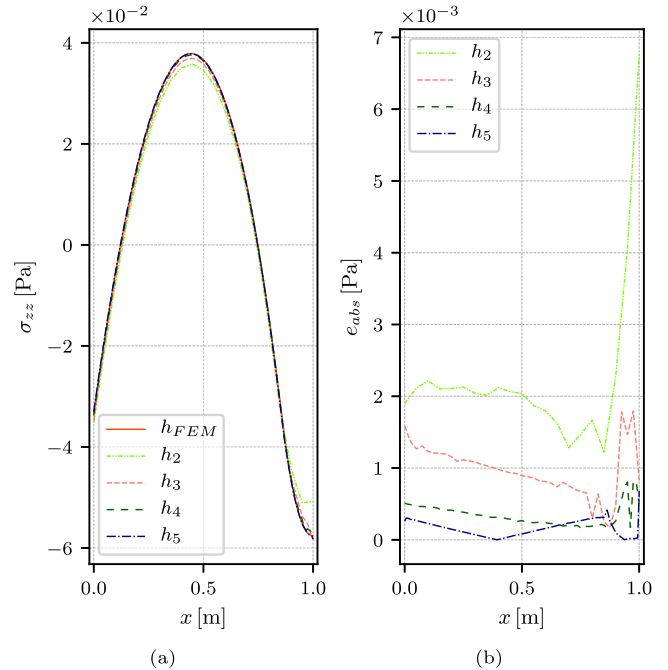


Fig. 14. SNA results of σ_{zz} over line $y = 0.25$ m (a) with corresponding absolute errors (b) for a generalised plane strain case.

the first time implemented within the hybrid RBF-FD method, where integral form constraints are included within RBF-FD for the first time.

The introduced solver is successfully validated on a simple benchmark where a reference solution was prepared with commercial FEM software.

The thermal solver was found to perform with the same accuracy on RNAs and SNAs where, as expected from previous studies [13], the h -convergence is governed by the augmentation order. No special treatment of the Neumann boundary conditions is needed. In [23],

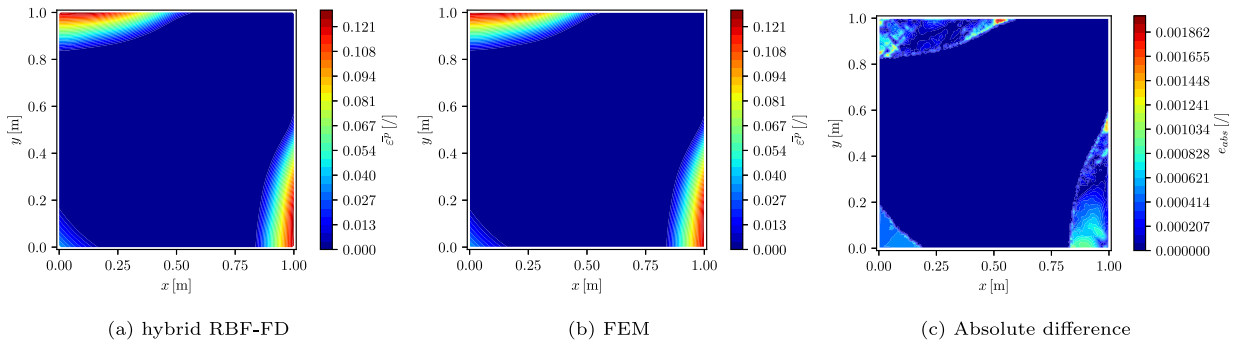


Fig. 15. Accumulated plastic strain solution for GPS. (a): SNA with h_5 . (b): reference solution obtained with FEM. (c): Absolute difference between solutions.

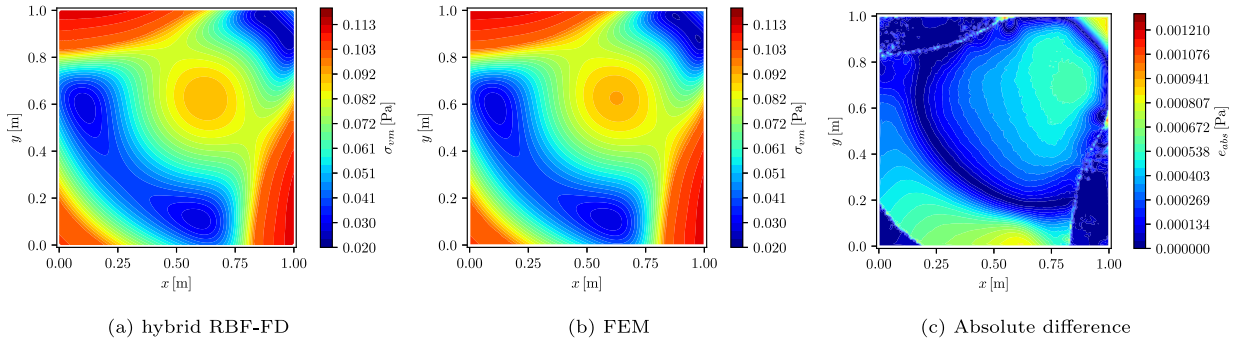


Fig. 16. Von Mises stress solution for GPS. (a): SNA with h_5 . (b): reference solution obtained with FEM. (c): Absolute difference between solutions.

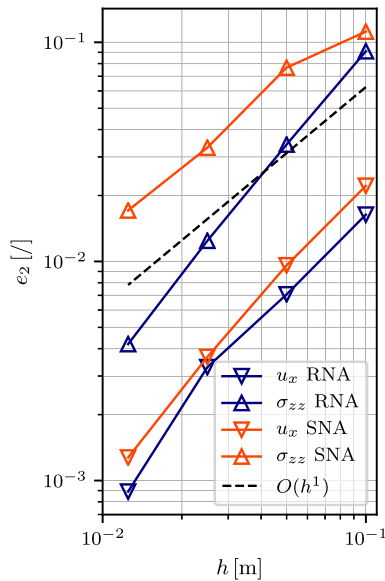


Fig. 17. h -convergence in u_x and σ_{zz} with RNA and SNA for the generalised plane strain case.

the heat diffusion equation was solved in a decoupled way with the nonlinear phase-field parabolic partial differential equation, where it was found that for the Euler scheme to be stable $\alpha_{\Delta t} \leq 0.3$. In this work, the same RBF-FD method was employed, and it was found that for only the heat diffusion equation, the time stability parameter can be larger $\alpha_{\Delta t} \leq 0.5$, where convergence in the time step is of the first order.

The mechanical solver was found to reproduce the reference solution successfully. At Neumann BCs, the non-smoothness in stress values is observed. This happens because temperature boundary values, computed in collocation nodes in the thermal model, are enforced on

shifted boundary nodes (empty squares in Fig. 4) in the mechanical model. This procedure enables evaluation of the exact temperature solution on the boundary but results in the non-smooth solution. If temperature values would be interpolated on shifted boundary nodes, then no jump in solution should be expected, but also, not the actual boundary values would be applied. The challenge of applying accurate boundary values while maintaining stability for Neumann BCs remains an open research question. The introduced non-smoothness decreases with increasing node arrangement density (and vanishes if no stabilisation is present). For the investigated cases, a stabilisation parameter $\alpha_S = 0.25$ was enough for the method to be stable. This also affected the h -convergence, where, except for the GPS cases with SNAs, it was found to be between the first and second orders. In GPS cases with SNAs, the convergence order is slightly reduced but not below the first order. The reason is that the area differentials needed in discretised integral equations are approximated with lower accuracy in the SNAs than in the RNAs, where they are exact.

As demonstrated, the one-way coupled thermo-elasto-plasticity can be successfully modelled using the proposed novel method. An example of its industrial application is provided in Part 2 of this publication for simulating the cooling of steel bars on a cooling bed in metallurgical processing.

Declaration of competing interest

The authors have no conflicts of interest to declare that are relevant to the content of this paper.

Data availability

Data will be made available on request.

Acknowledgements

This research was funded by the Slovenian Grant Agency by grant numbers P2-0162, L2-3173, and Z2-2640. The first author was supported by the Young Researcher's grant.

References

- [1] de Souza Neto EA, Peric D, Owen DR. *Computational methods for plasticity: Theory and applications*. Chichester, West Sussex, UK: John Wiley & Sons; 2011.
- [2] Cardiff P, Demirdžić I. Thirty years of the finite volume method for solid mechanics. *Arch Comput Methods Eng* 2021;28(5):3721–80. <http://dx.doi.org/10.1007/s11831-020-09523-0>.
- [3] Liu GR. *Meshfree methods: Moving beyond the finite element method, Second Edition*. Baton Rouge, Louisiana, USA: Taylor & Francis Group; 2009.
- [4] Šarler B, Atluri SN. *Recent studies in meshless and other novel computational methods*. Duluth, Minnesota, USA: Tech Science Press; 2010.
- [5] Pepper D, Kassab A, Divo E. *Introduction to finite element, boundary element, and meshless methods: With applications to heat transfer and fluid flow*. New York, USA: ASME Press; 2014. <http://dx.doi.org/10.1115/1.860335>.
- [6] Slak J. *Adaptive RBF-FD method (Ph.D. thesis)*, Ljubljana, Slovenia: University of Ljubljana; 2020.
- [7] Zamolo R, Nobile E, Sarler B. Novel multilevel techniques for convergence acceleration in the solution of systems of equations arising from RBF-FD meshless discretizations. *J Comput Phys* 2019;392:311–34. <http://dx.doi.org/10.1016/j.jcp.2019.04.064>.
- [8] Kargarnovin M, Ekhteraei Toussi H, Fariborz S. Elasto-plastic element-free Galerkin method. *Comput Mech* 2004;33(3):206–14. <http://dx.doi.org/10.1007/s00466-003-0521-5>.
- [9] Ji-fa Z, Wen-pu Z, Zheng Y. Meshfree method and its applications to elasto-plastic problems. *J Zhejiang Univ - Sci A: Appl Phys Eng* 2005;6(2):148–54. <http://dx.doi.org/10.1007/BF02847979>.
- [10] Zhang X, Song KZ, Lu MW, Liu X. Meshless methods based on collocation with radial basis functions. *Comput Mech* 2000;26(4):333–43. <http://dx.doi.org/10.1007/s004660000181>.
- [11] Tolstykh A, Shirobokov D. On using radial basis functions in a “finite difference mode” with applications to elasticity problems. *Comput Mech* 2003;33(1):68–79. <http://dx.doi.org/10.1007/s00466-003-0501-9>.
- [12] Šarler B, Vertnik R. Meshfree explicit local radial basis function collocation method for diffusion problems. In: *Radial Basis Functions and Related Multivariate Meshfree Approximation Methods: Theory and Applications*, *Comput Math Appl In: Radial Basis Functions and Related Multivariate Meshfree Approximation Methods: Theory and Applications*, 2006;51(8):1269–82. <http://dx.doi.org/10.1016/j.camwa.2006.04.013>.
- [13] Flyer N, Fornberg B, Bayona V, Barnett GA. On the role of polynomials in RBF-FD approximations: I. Interpolation and accuracy. *J Comput Phys* 2016;321(1):21–38. <http://dx.doi.org/10.1016/j.jcp.2016.05.026>.
- [14] Vertnik R, Šarler B. Meshless local radial basis function collocation method for convective-diffusive solid-liquid phase change problems. *Internat J Numer Methods Heat Fluid Flow* 2006;16(5):617–40. <http://dx.doi.org/10.1108/09615530610669148>.
- [15] Kosec G, Šarler B. Solution of a low Prandtl number natural convection benchmark by a local meshless method. *Internat J Numer Methods Heat Fluid Flow* 2013;23(1):22. <http://dx.doi.org/10.1108/09615531311289187>.
- [16] Vertnik R, Šarler B. Local collocation approach for solving turbulent combined forced and natural convection problems. *Adv Appl Math Mech* 2011;3:259–79. <http://dx.doi.org/10.4208/aamm.10-10s2-01>.
- [17] Mramor K, Vertnik R, Šarler B. Meshless approach to the large-eddy simulation of the continuous casting process. *Eng Anal Bound Elem* 2022;138:319–38. <http://dx.doi.org/10.1016/j.enganabound.2022.03.001>.
- [18] Mramor K, Vertnik R, Sarler B. Development of Three-Dimensional LES Based Meshless Model of Continuous Casting of Steel. *Metals* 2022;12:1750. <http://dx.doi.org/10.3390/met12101750>.
- [19] Mramor K, Vertnik R, Šarler B. Simulation of continuous casting of steel under the influence of magnetic field using the local-radial basis-function collocation method. *Mater Technol* 2014;48:281–8.
- [20] Mramor K, Vertnik R, Šarler B. Application of the local RBF collocation method to natural convection in a 3D cavity influenced by a magnetic field. *Eng Anal Bound Elem* 2020;116(17–18):1–13. <http://dx.doi.org/10.1016/j.enganabound.2020.03.025>.
- [21] Kosec G, Šarler B. Simulation of macrosegregation with mesosegregates in binary metallic casts by a meshless method. *Eng Anal Bound Elem* 2014;45:36–44. <http://dx.doi.org/10.1016/j.enganabound.2014.01.016>.
- [22] Lehto E, Shankar V, Wright G. A radial basis function (RBF) compact finite difference (FD) scheme for reaction-diffusion equations on surfaces. *SIAM J Sci Comput* 2017;39(5):A2129–51. <http://dx.doi.org/10.1137/16M1095457>.
- [23] Dobravec T, Mavrič B, Šarler B. Reduction of discretisation-induced anisotropy in the phase-field modelling of dendritic growth by meshless approach. *Comput Mater Sci* 2020;172(1):109166. <http://dx.doi.org/10.1016/j.commatsci.2019.109166>.
- [24] Dobravec T, Mavrič B, Sarler B. Phase field modelling of dendritic solidification by using an adaptive meshless solution procedure. *IOP Conf Ser: Mater Sci Eng* 2020;861:012060. <http://dx.doi.org/10.1088/1757-899X/861/1/012060>.
- [25] Bayona V, Sanchez-Sanz M, Fernández-Tarrazo E, Kindelan M. Micro-combustion modelling with RBF-FD: A high-order meshfree method for reactive flows in complex geometries. *Appl Math Model* 2021;94(2–3):635–55. <http://dx.doi.org/10.1016/j.apm.2021.01.032>.
- [26] Hatić V, Rek Z, Mramor K, Mavrič B, Sarler B. A meshless solution of a of lid-driven cavity containing a heterogeneous porous medium. In: *IOP conference series: Materials science and engineering*, vol. 861, Jönköping, Sweden; 2020, 012028. <http://dx.doi.org/10.1088/1757-899X/861/1/012028>.
- [27] Hatić V, Mavrič B, Sarler B. Meshless simulation of a lid-driven cavity problem with a non-Newtonian fluid. *Eng Anal Bound Elem* 2021;131:86–99. <http://dx.doi.org/10.1016/j.enganabound.2021.06.015>.
- [28] Rana K, Mavrič B, Zahoor R, Sarler B. A meshless solution of the compressible viscous flow in axisymmetric tubes with varying cross-sections. *Eng Anal Bound Elem* 2022;143:340–52. <http://dx.doi.org/10.1016/j.enganabound.2022.06.029>.
- [29] Thakoor N, Tangman Y, Bhuruth M. RBF-FD schemes for option valuation under models with price-dependent and stochastic volatility. *Eng Anal Bound Elem* 2017;92. <http://dx.doi.org/10.1016/j.enganabound.2017.11.003>.
- [30] Xu W-Z, Fu Z-J, Xi Q. A novel localized collocation solver based on a radial Trefftz basis for thermal conduction analysis in FGMs with exponential variations. *Comput Math Appl* 2022;117:24–38. <http://dx.doi.org/10.1016/j.camwa.2022.04.007>, URL <https://www.sciencedirect.com/science/article/pii/S0898122122001560>.
- [31] Fu Z, Tang Z, Xi Q, Liu Q, Gu Y, Wang F. Localized collocation schemes and their applications. *Acta Mech Sin* 2022;38(7):422167. <http://dx.doi.org/10.1007/s10409-022-22167-x>, URL <https://doi.org/10.1007/s10409-022-22167-x>.
- [32] Stevens D, Power H, Cliffe K. A solution to linear elasticity using locally supported RBF collocation in a generalised finite-difference mode. *Eng Anal Bound Elem* 2013;37(1):32–41. <http://dx.doi.org/10.1016/j.enganabound.2012.08.005>.
- [33] Ferreira AJM, Roque CMC, Martins PALS. Analysis of composite plates using higher-order shear deformation theory and a finite point formulation based on the multiquadric radial basis function method. *Composites B* 2003;34(7):627–36. [http://dx.doi.org/10.1016/S1359-8368\(03\)00083-0](http://dx.doi.org/10.1016/S1359-8368(03)00083-0).
- [34] Ferreira AJM, Fasshauer GE. Computation of natural frequencies of shear deformable beams and plates by an RBF-pseudospectral method. *Comput Methods Appl Mech Engrg* 2006;196(1):134–46. <http://dx.doi.org/10.1016/j.cma.2006.02.009>.
- [35] Gerace S, Divo E, Kassab A. A localized radial-basis-function meshless method approach to axisymmetric thermo-elasticity. San Francisco, California, USA; 2006. <http://dx.doi.org/10.2514/6.2006-3788>.
- [36] Mavrič B, Šarler B. A collocation meshless method for linear thermoelasticity in 2D. In: *3rd international conference on computational methods for thermal problems, thermacomp 2014*, Bled, Slovenia; 2014, p. 279–82.
- [37] Mavrič B. *Meshless modeling of thermo-mechanics of low-frequency electromagnetic direct chill casting (Ph.D. thesis)*, Nova Gorica, Slovenia: University of Nova Gorica; 2017.
- [38] Hanoglu U, Islam S-u-I, Šarler B. Thermo-mechanical analysis of hot shape rolling of steel by a meshless method. *Procedia Eng* 2011;10:3181–6. <http://dx.doi.org/10.1016/j.proeng.2011.04.524>.
- [39] Hanoglu U, Šarler B. Simulation of hot shape rolling of steel in continuous rolling mill by local radial basis function collocation method. *CMES Comput Model Eng Sci* 2015;109–110(5):447–79. <http://dx.doi.org/10.3970/cmesc.2015.109.447>.
- [40] Hanoglu U, Šarler B. Multi-pass hot-rolling simulation using a meshless method. *Comput Struct* 2018;194:1–14. <http://dx.doi.org/10.1016/j.compstruc.2017.08.012>.
- [41] Hanoglu U, Šarler B. Hot rolling simulation system for steel based on advanced meshless solution. *Metals* 2019;9(7):788. <http://dx.doi.org/10.3390/met907788>.
- [42] Cacciani N, Larsson E, Lauro A, Meggiolaro M, Scatto A, Tominec I, Villard P-F. A First Meshless Approach to Simulation of the Elastic Behaviour of the Diaphragm. In: *Sherwin SJ, Moxey D, Peiró J, Vincent PE, Schwab C, editors. Spectral and high order methods for partial differential equations ICOSAHOM 2018*. Lecture notes in computational science and engineering, Cham, Switzerland: Springer International Publishing; 2020, p. 501–12. http://dx.doi.org/10.1007/978-3-030-39647-3_40.
- [43] Strniša F, Jančić M, Kosec G. A meshless solution of a small-strain plasticity problem. In: *2022 45th Jubilee international convention on information, communication and electronic technology (MIPRO)*, Opatija, Croatia; 2022, p. 257–62. <http://dx.doi.org/10.23919/MIPRO55190.2022.9803585>.
- [44] Mavrič B, Dobravec T, Vertnik R, Šarler B. A meshless thermomechanical travelling-slice model of continuous casting of steel. In: *IOP conference series: materials science and engineering*, 012018, vol. 861, Jönköping, Sweden; 2020. <http://dx.doi.org/10.1088/1757-899X/861/1/012018>.
- [45] Vuga G, Mavrič B, Šarler B. An improved local radial basis function method for solving small-strain elasto-plasticity. *Comput Methods Appl Mech Engrg* 2024;418:116501. <http://dx.doi.org/10.1016/j.cma.2023.116501>, URL <https://www.sciencedirect.com/science/article/pii/S0045782523006254>.
- [46] Fornberg B, Flyer N. Fast generation of 2-D node distributions for mesh-free PDE discretizations. *Comput Math Appl* 2015;69(7):531–44. <http://dx.doi.org/10.1016/j.camwa.2015.01.009>, URL <https://www.sciencedirect.com/science/article/pii/S0898122115000334>.
- [47] Smith M. *Abaqus/Standard User's Manual, Version 6.9*. 2009.